The Astrophysical Journal, 969:91 (15pp), 2024 July 10 https://doi.org/10.3847/1538-4357/ad41dd

The Distribution of Pc5 Ultralow-frequency Waves at Geostationary Orbit

Paul T. M. Loto'aniu[1,2] and F. Inceoglu[1,2]
[1] Cooperative Institute for Research in Environmental Sciences, University of Colorado Boulder Boulder, CO, USA; paul.lotoaniu@noaa.gov
[2] National Centers for Environmental Information, National Oceanic and Atmospheric Administration Boulder, CO, USA
Received 2023 December 29; revised 2024 April 1; accepted 2024 April 21; published 2024 July 2

Abstract

Using GOES magnetometer data spanning over 30 yr, we study the distribution of Pc5 ultralow-frequency waves at geosynchronous orbit. The CLEAN algorithm was applied to detect narrowband Pc5 waves. This method was first used in astronomical radio interferometry, but has since been applied to many other areas. The algorithm allows for identification of multiple individual peaks within the same power spectral density. We found close to 30,000 events in each magnetic field component in field-aligned coordinates. With some exceptions, results were in agreement with previous studies. Wave occurrence along magnetic local time (MLT) was higher in the 18–23 MLT sector. However, the largest accumulated wave amplitudes were observed on the dayside, peaking close to local noon. As expected, wave amplitudes were larger during more active solar wind conditions. For the radial and parallel components, amplitudes were maximum at the interplanetary magnetic field clock angle of −30° to −45°. The resultant database of Pc5 ultralow-frequency wave events can be used to constrain radiation belt models, while the CLEAN method provides a unique technique to automatically detect narrowband plasma waves in the magnetosphere and beyond.

Unified Astronomy Thesaurus concepts: Planetary magnetospheres (997); Alfvén waves (23); Space weather (2037); Van Allen radiation belts (1758)

1. Introduction

Ultralow-frequency (ULF) waves are among the most studied plasma waves in Earth's magnetosphere. These waves are important for both basic plasma physics research and space weather research because they are thought to play an important role in the dynamics of radiation belt electrons. The Pc5 (continuous pulsation 5) band of the ULF wave range covers about 1.7–7 mHz (Jacobs et al. 1964; Menk 2011), and these waves are generally global mode magnetic field oscillations with the solar wind as the external energy source for wave generation. However, even after decades of research there is no well-accepted model for how the solar wind excites these ULF waves in the magnetosphere.

Statistical properties of the ULF waves are important in radiation belt physics. The wave mode, frequency, power, local time occurrence, and duration all influence the strength and type of wave–particle interactions and therefore the role ULF waves plays in acceleration of relativistic electrons. Numerous statistical studies have been undertaken to characterize the global occurrence, spectral, spatial, and temporal characteristics of Pc5 ULF waves (e.g., Kokubun 1985; Anderson et al. 1990; Zhu & Kivelson 1991; Cao et al. 1994; Lessard et al. 1999; Hudson et al. 2004; Takahashi & Ukhorskiy 2007; Liu et al. 2009; Wang et al. 2015; Murphy et al. 2020b; Sarris et al. 2022).

These studies can generally be separated into ones that looked at narrowband waves and those that studied broadband noise. As a recent example, Sarris et al. (2022) used THEMIS and Arase Mission magnetic field data to determine the integrated power of ULF waves over the Pc4 / Pc5 (1.7–22.2 mHz) range using wavelet transformations. This method of determining the power spectral density (PSD) using either fast Fourier transformations (FFTs) or wavelets, then integrating to get total power over a wave band or integrating then averaging the power over a time or spatial interval, is a commonly employed technique in broadband statistical studies.

In order to improve our understanding of wave-generation mechanisms and propagation characteristics, statistical studies of narrowband waves are also important. Again, to give a recent example, Murphy et al. (2020b) used 4 yr of observations from the GOES-15 mission to investigate the distribution and occurrence of both broadband and narrowband ULF waves. Note that Murphy et al. use the word "discrete," but in this study we shall refer to narrowband rather than discrete ULF waves because the latter term is often used when ULF wave power peaks at preferred frequencies. Murphy et al. used the Automated Flare Inference of Oscillations (AFINO) algorithm (Inglis et al. 2015, 2016), which was developed to identify quasiperiodic pulsations in solar flares. The AFINO algorithm uses spectral models to fit the FFT-based PSD, with a power law identifying broadband and a power law plus extra term corresponding to a Gaussian enhancement for fitting narrowband events. A disadvantage of the AFINO method is that it cannot identify multiple individual peaks within the same PSD and it is dependent on a model fit, which may not be a good representation of the wave power.

Here, we use almost 30 yr of GOES magnetic field data to identify narrowband Pc5 ULF waves at geostationary orbit. This is the longest historical data set used to date in the statistical study of ULF waves in space. Although the GOES orbit is restricted in L shell compared to elliptical orbiting spacecraft, the persistent measurements over multiple decades makes this data set very appealing for studying waves during different solar cycles (SCs). In addition, with the GOES orbit being on the outer edge of the radiation belt, wave spectral properties extracted from these observation can provide radial diffusion boundary conditions for radiation belt models.

This study introduces the CLEAN (Högbom 1974) algorithm to identify Pc5 narrowband waves or individual wavepackets. The CLEAN method was first used for constructing 2D images in astronomical radio interferometry, but has since been applied to a huge range of areas (Cornwell 2009) including adaptation for time series analysis (Roberts et al. 1987). The algorithm performs a nonlinear deconvolution in the frequency domain (equivalent to a least-squares regression in the time domain) allowing for identification of multiple individual peaks within the same PSD. The CLEAN method also produces real amplitudes instead of model fits, and phase information is retained.

In Section 2, we describe the data set used, while in Section 3, the methodology is explained, including the steps within the CLEAN method. The results are presented in Section 4, and a discussion given in Section 5. Finally, Section 6 presents our conclusions.

2. Data

The National Oceanic and Atmospheric Administration (NOAA) Geostationary Operational Environmental Satellites (GOES) have been providing continuous observations of Earth's magnetic field at geostationary orbit since 1975 (Singer et al. 1996; Loto'aniu et al. 2019a, 2019b). In our study, we used 1 minute resolution magnetic field data (referred to as MAG data) from multiple GOES satellites (GOES-08 to GOES-17) covering the period from 1995 July 1 to 2023 March 1. The data were taken from NOAA's National Centers for Environmental Information (NCEI) public data servers.[3] MAG measurements are most commonly available in the local spacecraft EPN coordinate system. In the EPN system, the *E*-axis is Earthward (nadir), the *P*-axis is normal to the orbital plane (poleward), and the *N*-axis (normal) completes the right-handed system (Loto'aniu et al. 2019b; Inceoglu & Loto'aniu 2021).

The magnetic field data are then converted from EPN to the mean field–aligned (MFA) coordinate frame. The MFA frame has its *x*-axis (B_r or the radial component) pointed outward from Earth and the *z*-axis ($B_{||}$ or the compressional component) aligned with Earth's dipolar unperturbed magnetic field. The *y*-axis (B_ϕ, the eastward or azimuthal component) is the cross product of the *x*-axis and Earth's magnetic dipole axis, defined as positive toward dusk magnetic local time (MLT). The mean field is defined as the 30 minute moving average of the total field. Following coordinate transformation, the data are sorted by MLT and highpass filtered using a fifth-order Butterworth filter with a 30 minute cutoff.

3. Methods

As previously mentioned, the CLEAN algorithm has been applied in many domains, including for deconvolution of time series data in the frequency domain (Roberts et al. 1987). In this study, we have once more repurposed this method to identify ULF wave signals in magnetic field data from GOES missions. Similarly to Murphy et al. (2020a), we use a moving 1 hr window with an overlapping 30 minute interval. The method works as follows:

1. First, the FFT of the input MAG data is calculated. A Hanning window is also applied to minimize aliasing effects.
2. In order to test statistical significance, 10,000 white noise signals with the same mean and standard deviation as the input MAG data are generated, followed by calculation of their FFTs.
3. Following that, we find the highest peak in the FFT of the input signal. If the wave amplitude a_p is above a minimum threshold value of 0.5 nT, we note the peak frequency as ω_p. The threshold value 0.5 nT was chosen in order to minimize the likelihood of artificial noise (e.g., instrument heater noise) in the GOES magnetometer data showing up in the results. If this signal is statistically significant at a level of $\rho < 0.05$ and is within the Pc5 interval of $1.6\,\mathrm{mHz} \leqslant \omega_p \leqslant 6.7\,\mathrm{mHz}$, its frequency, amplitude, and phase are registered as a ULF wave signal. Then the power at $\omega_p \pm 4\delta\omega$ range is equated to 0, where $\delta\omega$ is the frequency resolution of the FFT. The width of $\pm 4\delta\omega$ was chosen in order to be wide enough to remove the shoulders of the spectral signal. It should be noted that, even if the signal does not satisfy our statistically significant ULF wave criteria, it is still removed from the FFT, but in such a case it is not registered as a ULF wave.
4. Then, the residual time series is calculated by taking the inverse of the FFT.
5. Finally, this process is run in a loop to detect any further FFT peaks until there is no statistically significant peak with an amplitude greater than 0.5 nT found. This is a process of finding multiple wave harmonics.

Figure 1(a) shows a day of artificial signals at 1 minute cadence composed of multiple sine waves. The amplitudes and power are shown in arbitrary units. Following the CLEAN method described above, we select the first hour of the time series (red box in panel (a) and expanded in panel (c)) and take the FFT. Panels (b) and (d) show the FFT without and with a Hanning window applied to the data, respectively. The Hanning window creates a broadening of the spectra, with the total area under the curve giving the power or amplitude of the wave. Although the Hanning window is not required in this artificial example, when using real measurements, applying this type of window is necessary to minimize unrealistic peaks such as Gibbs phenomena.

We then take the FFTs of 10,000 white noise signals with the same mean and standard deviation as the input data, shown as the gray region in panel (d). Statistical properties of the highest peak in the spectrum that is above 0.5 nT, within the Pc5 frequency range and statistically significant at a $\rho < 0.05$ level, are saved. The peak is then removed from the spectrum, and the inverse FFT applied to the remaining signal, with the resultant residual time series shown in panel (e). The above steps are repeated iteratively until there is no signal in the FFTs that satisfies the selection criteria (panels (e) and (g)).

4. Results

Applying our method to the magnetic field data spanning almost 30 yr and multiple GOES missions resulted in 26,920 ULF wave signals in B_r, 27,176 in B_ϕ, and 32,880 in $B_{||}$ components in the MFA frame. Figure 2 shows an example of the CLEAN method applied to a harmonic Pc5 event observed

[3] https://www.ncei.noaa.gov/

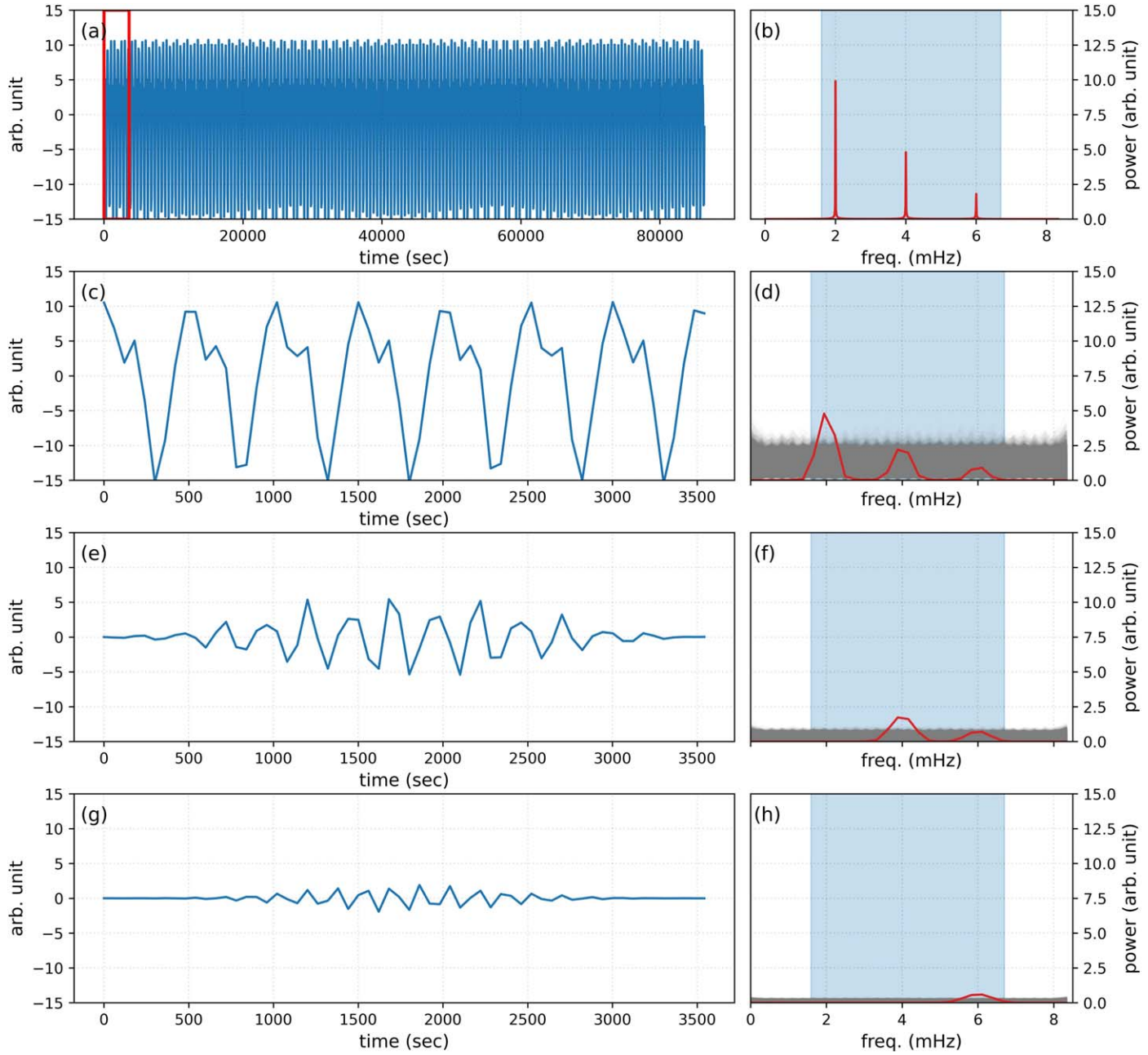

Figure 1. Panel (a) shows the generated signal while the panel (b) shows its FFT. The blue shaded areas in (b) and the panels below it show the 1.6–6.7 mHz region for Pc5 ULF waves. We also show the selected 1 hr window (red box) and how the CLEAN algorithm works. The left panels shows the generated signal (c) and each data residual after signal extraction ((e) and (g)). The right panels show the Fourier transformations of the original signal (d) and each of the residual data after signal extraction ((f) and (h)). The gray shaded areas show Fourier transformation of the 10,000 white noise signals.

by GOES-16. Panel (a) shows 24 hr of the magnetic field radial component time series and the corresponding dynamic spectra. Using 1 hr of data enclosed in the dotted rectangle, which is expanded in panel (b), the CLEAN algorithm outputs are shown in panels (c)–(i).

The highest-amplitude peak is recorded between 2 and 3 mHz (panel (c)), then removed with the residual time series shown in panel (d) and the FFT reapplied (panel (e)). The next highest peak is removed but not recorded because it is observed outside the Pc5 range (panels (f) and (g)). The residual signal has one peak above the significance level between 4 and 6 mHz, and this peak is recorded and removed. No remaining peaks meet the selection criteria (panels (h) and (i)).

In terms of overall statistics, the top panels in Figure 3 show the ULF wave occurrences for each component in MLT, where the radial distance represents number of events. The bottom panels show the component logarithmic cumulative wave amplitudes as a function of MLT and wave frequency. If we consider "high occurrence" to mean 1500 or more events, for B_r this occurs mainly between 19 and 23 MLT and for B_ϕ 21–23 MLT. The parallel component, $B_{||}$, shows a wider high-occurrence region of 13–23 MLT.

Defining "low occurrence" to mean less than 1000 events, this was observed across a wide local time for B_r of 07–16 MLT but a more narrow 06–10 MLT for B_ϕ and 06–09 MLT for $B_{||}$. Interestingly, 24 MLT is a low-occurrence

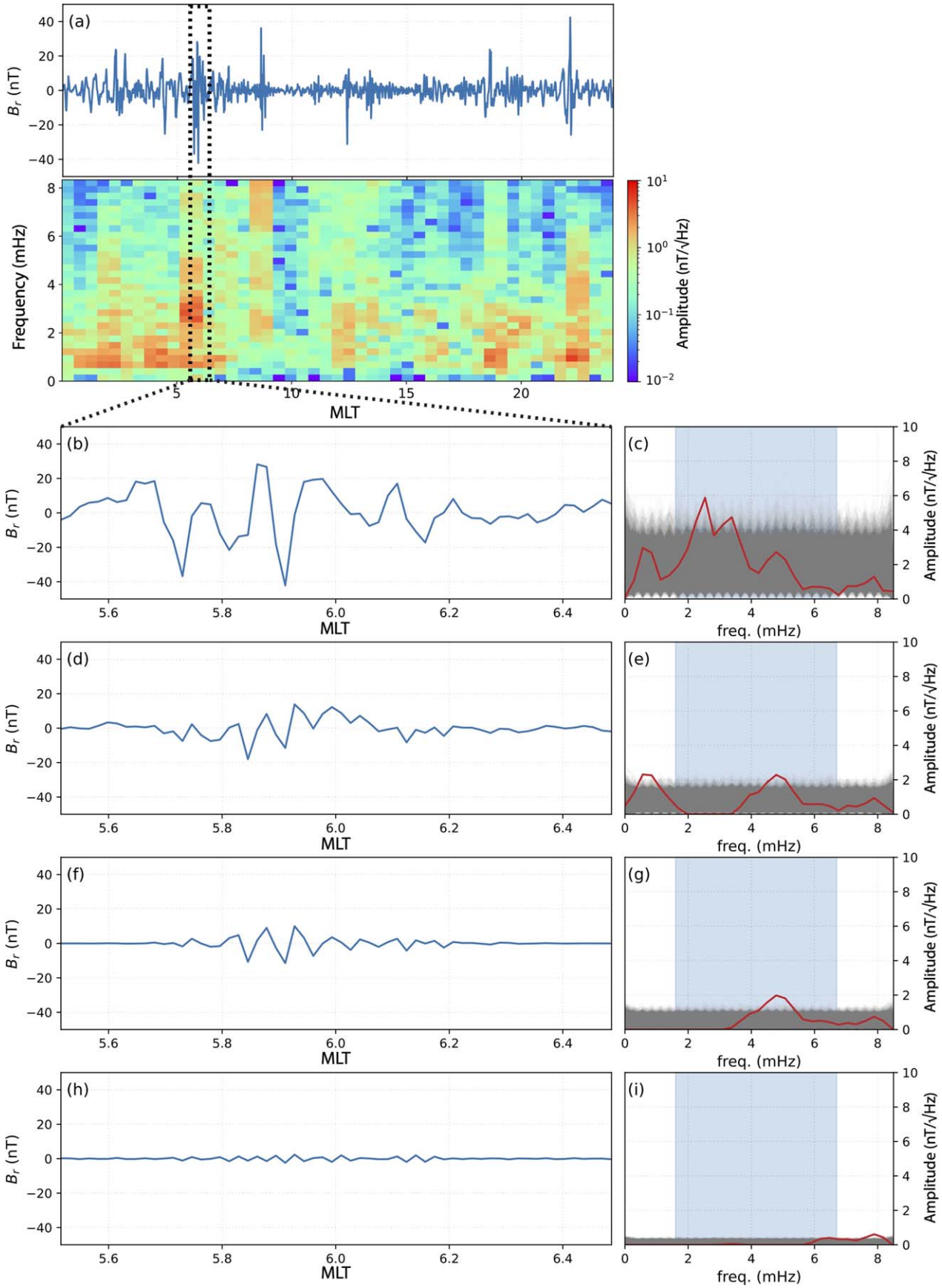

Figure 2. Example of the CLEAN method applied to a harmonic Pc5 event observed by GOES-16 on 2023 February 27. Panel (a) shows 24 hr of the magnetic field radial component time series and the corresponding dynamic spectra. The CLEAN algorithm is applied to the data enclosed in the dotted rectangle, which is expanded in panel (b), with results shown in panels (c)–(i).

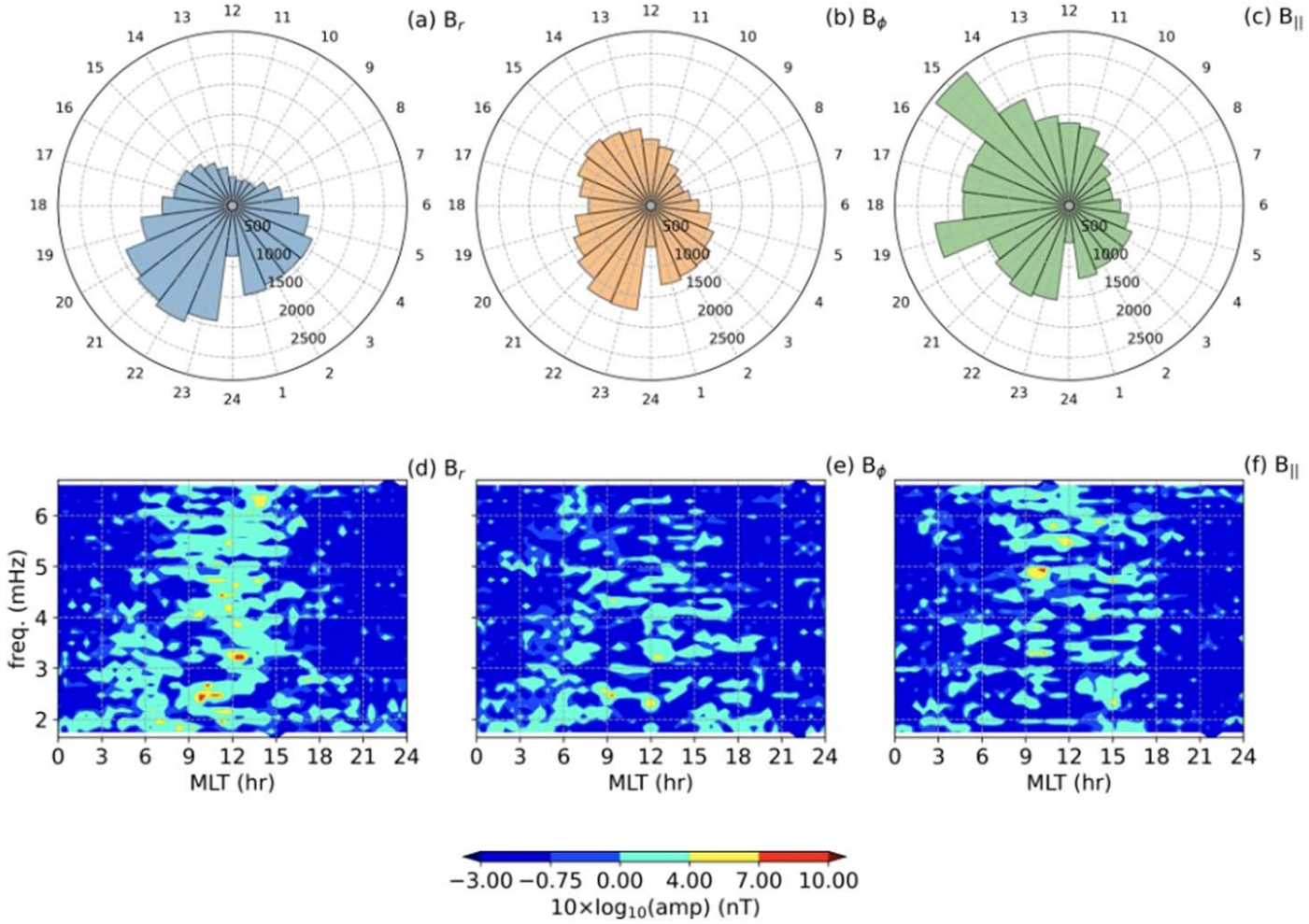

Figure 3. The top panel shows the total number of occurrences of the ULF waves found in GOES magnetometer data spanning from 1995 July 1 to 2023 March 1. The panels (a), (b), and (c) show the total number of ULF waves found in the radial, azimuthal, and compressional components of the magnetic field in MFA frame as a function of the MLT. The bottom panel shows the cumulative amplitudes and frequencies of all the ULF waves found for the same period in the radial (d), azimuthal (e), and compressional (f) components as a function of the MLT and frequency.

hour for all three components, and this was observed across all statistics irrespective of what parameter was used to separate events. Another interesting result is that, for $B_{||}$, 15 and 19 MLT each show a spike in occurrence. This phenomena is also observed for $B_{||}$ under all solar wind conditions that were studied.

For B_r, even though the higher occurrence tends to be in the local nighttime sector, this region generally has weaker-amplitude events (see panel (d)), with a maximum of about 2.5 nT. Most of the B_r wave amplitudes lie between about 03–15 MLT, where maximum amplitudes can reach beyond 10 nT, especially between 09 and 15 MLT. At lower frequencies, wave amplitudes tend to be spread across more MLT. The azimuthal component, B_ϕ, has lower amplitudes that are not as concentrated in MLT as B_r but mostly restricted to 03–21 MLT, especially at higher frequencies. The $B_{||}$ component amplitudes are also lower, on average, with amplitudes generally within 03–18 MLT.

We note that care should be taken when visually comparing different-amplitude spectra. In order to produce a smooth spectra from the individual amplitudes making up the frequency/MLT grid, nearest-neighbor interpolation was applied to the values. As a result, in the following sections, the reader will notice that amplitude spectra using a subset of the total events can show higher amplitudes than the spectra using the entire data set shown in Figure 3. The reason why is best illustrated with this simple example: the average of a grid composed of two values, 10 and 10, is higher than the average of a three-point grid composed of 10, 10, and 1, even though the peak individual amplitudes of the two grids are the same, i.e., 10. Hence, having more data tends to result in lowering the interpolated-amplitude spectra.

4.1. Differences in Solar Cycles 23 and 24

The time span of our study extends for two full SCs and covers the inclining phase of SC-25. Since the solar cycle amplitudes declined from SC-23 to SC-24, we separated the events into two cycles to compare distributions and amplitudes, as shown in Figure 4, with panels (a)–(f) showing SC-23 results and panels (g)–(l) SC-24 results. The occurrence patterns across MLTs were similar for the two solar cycles and also matched the combined data set shown in Figure 3, except of course that the number of events in SC-23 is significantly higher than that in SC-24. For example, the number of B_r events at 22 MLT during SC-23 was around 1100, while for SC-24 at 22 MLT it was lower at close to 700. The higher number of events in SC-23 is not unexpected, since that solar

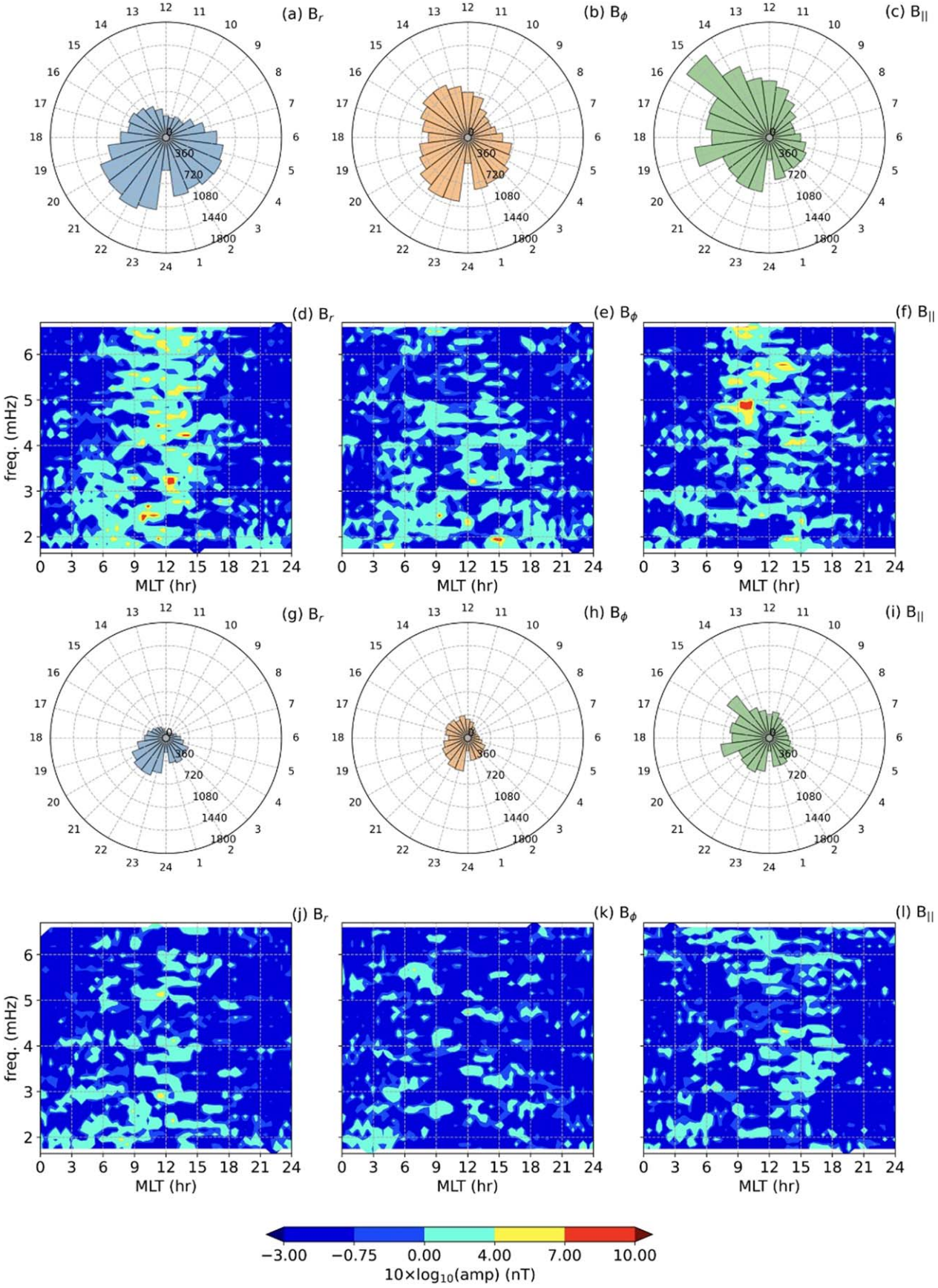

Figure 4. Panels (a)–(f) show wave occurrence and amplitudes during SC-23, and panels (g)–(l) show the same for SC-24. See text for further explanations.

cycle was more active, with higher Sunspot numbers at its peak, than SC-24.

With regard to wave amplitudes, in SC-23, all three magnetic field components show minimal wave amplitudes in the evening sector from about 18 to 03 MLT, in particular at higher frequencies. For both the radial and parallel components, during SC-23, peak wave amplitudes occurred between about 09 and 15 MLT across most frequencies (Figures 4(d) and (f)). The peak amplitudes in the azimuthal component were from about 03 to 18 MLT (Figure 4(e)), but tended to be lower in amplitude across both MLT and frequency compared to the other two components. Comparing wave amplitudes between SC-23 and SC-24, the cumulative amplitudes during SC-23 could be several orders of magnitude higher than that observed on SC-24. As with the occurrences, this is not unexpected, since SC-23 was a more active solar cycle. Also, the time intervals that tend to show the smallest wave amplitudes across all frequencies are found in the sector from about 18 to 03 MLT (Figures 4(j), (k), and (l)).

4.2. Differences with Solar Wind Parameters

We also looked at the distribution of wave event occurrence under different solar wind conditions; interplanetary magnetic field (IMF) strength (IMF B_z); solar wind speed (V_{sw}); and solar wind density. Figure 5 shows the occurrence and amplitudes for IMF $B_z \leqslant -5$ nT (top two rows) and 5 nT $>$ IMF B_z > -5 nT (bottom two rows). These two conditions represent strong negative IMF B_z and moderate solar wind IMF B_z conditions, respectively.

It should be noted that, in Figure 5, the number of events along the radial direction in the polar occurrence panels do not have the same scale between the strong and moderate IMF B_z conditions. The moderate IMF B_z occurrence panels have a scale maximum of 3000, while the strong IMF B_z occurrence panels have a maximum scale 10 times lower. There are on average about 10 times more events during moderate IMF B_z, which is a function of the fact that the average IMF B_z is 0 nT with a mode within one standard deviation of the average and both statistical values lie in the moderate range. In other words, over the time range of this data set, the IMF B_z was moderate, on average. Because of this, the shape of the occurrence distribution for all three components during moderate conditions is very similar to the distribution of all events.

Under strong negative IMF B_z conditions, the Pc5 wave occurrence for the radial and azimuthal components both peak close to dawn at 04–05 MLT, while the $B_{||}$ occurrence is also enhanced at 04 MLT but peaks in the afternoon sector between 13 and 15 MLT. Like the results for all events, the B_r amplitudes tend to maximize around local noon for both moderate and strong IMF B_z conditions, except that, during strong negative IMF B_z, there are peaks in amplitudes at low frequencies <2 mHz between about 03–10 MLT and 15–21 MLT. We also observe the tendency for amplitudes to be more restricted within 06–15 MLT at higher frequencies. The $B_{||}$ maximum amplitudes again tend to be clustered around local noon. There is no clear pattern for B_ϕ, although at low frequencies the maximum amplitudes tend to be on the flanks.

Figures 6 and 7 show the occurrence and amplitudes, respectively, separated by solar wind speed with high speed defined as $V_{sw} \geqslant 500$ km s^{-1}, moderate speed as 500 km s^{-1} $>$ v_{sw} $>$ 350 km s^{-1}, and slow speed $V_{sw} \leqslant 350$ km s^{-1}. We should note that the occurrence range in the radial direction for the $V_{sw} \leqslant 350$ km s^{-1} case (lower row of panels in Figure 6) is smaller (0–250) than those for the higher-speed occurrence plots, which both have a range of 0–1500. The significantly lower number of events during low solar wind speeds is expected because increased geomagnetic activity is generally associated with elevated speeds.

The occurrence during high solar wind speeds is consistent with the distribution for all events shown in Figure 3. For moderate conditions, the peaks in occurrence were also located at similar MLTs. However, $B_{||}$ under moderate conditions showed a bias toward more events in the 14–19 MLT sector.

Looking at the corresponding amplitude plots in Figure 7, we observe that Pc5 wave amplitudes are low during low solar wind speed. The amplitude results for moderate and high solar wind speeds are somewhat similar, except that for moderate conditions, B_r and $B_{||}$ tend to be more restricted in MLT to the day sector, while the amplitudes are overall lower for B_ϕ. In the case of B_r, there is a tendency for peak amplitudes to shift from early MLT at low frequencies to around local noon at higher frequencies. For $B_{||}$, peaks at local noon are also more prominent at higher frequencies.

Figure 8 shows the occurrence and amplitudes for two cases of solar bulk density ($\geqslant 7/\text{cm}^{-3}$ and $<7/\text{cm}^{-3}$). For low densities, the relative occurrence across MLT is similar to the MLT distribution for all events, while for high-density periods, there is a relative decrease in events in the dusk-to-midnight sector versus a relative increase in events in the post-noon sector. The statistical mode lies in the low-density region, which is likely the reason why the low-density distribution pattern is similar to the occurrence for all events. The amplitude distribution during high densities resembles the case for high solar wind speeds, while the low-density periods have much lower amplitudes.

Figures 9 and 10 show the Pc5 wave amplitudes binned into different 15° IMF clock angles and cone angles, respectively. The clock angle is defined as $\tan^{-1}(B_y/B_z)$ and the cone angle as $\cos^{-1}(B_x/B_t)$, where B_t is the total IMF. In our definition, a clock angle of $<0°$ means southward IMF and $>0°$ means the IMF is oriented northward, while a cone angle of 0° means the IMF points along –Xgse and the range is 0°–180°, with 180° representing the IMF along the +Xgse direction or pointing toward the Sun.

In the interest of saving space, we only show the angles needed to explain the results. The Pc5 wave amplitudes are enhanced during IMF clock angles within about ±45°, and amplitudes peak around −30° to −45°. These maximum amplitudes are most pronounced for the radial and parallel component and around local noon. Wave amplitudes are minimal for IMF clock angles around ±90°.

For the IMF cone angles, the Pc5 wave amplitudes maximize around 90° ± 15° and drop off outside of this range. However, the peaks do not reach as high as observed for IMF clock angle. This suggests that IMF clock angle has a stronger influence on Pc5 wave amplitudes compared to IMF cone angle. In terms of distribution of amplitudes with frequency, there was not an obvious difference between clock and cone angles.

The occurrence as a function of clock and cones angles (results not shown) were similar for all components. The maximum occurrence was for clock angles around ±90°, with minimum about 0° and more events occurring during negative IMF B_z. For cone angle, minimum occurrence was at close to

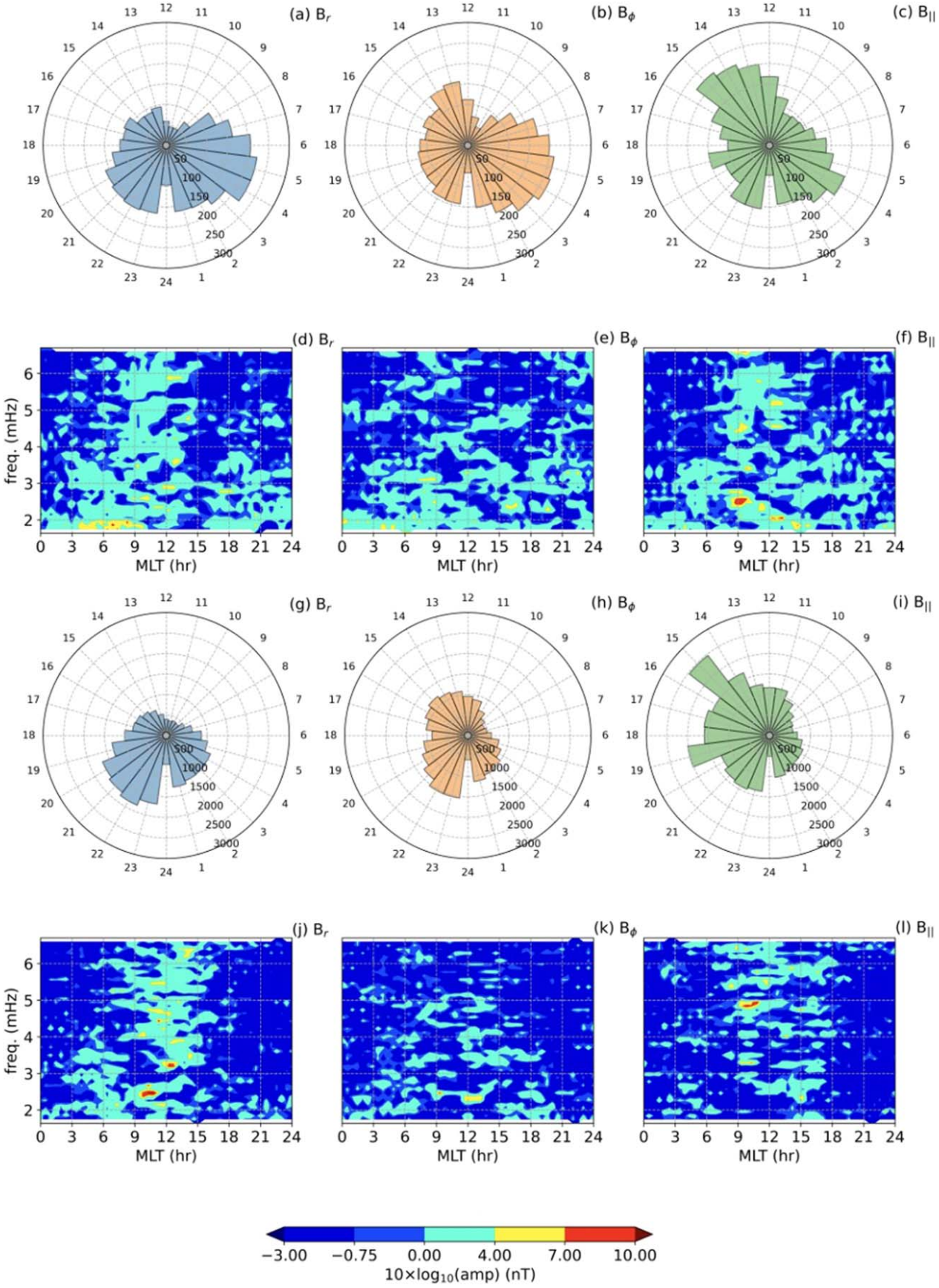

Figure 5. Occurrence rates and amplitudes for different IMF B_z. Panels (a)–(f) show those for $B_z \leqslant -5$ nT, and (g)–(l) show those for 5 nT $> B_z > -5$ nT.

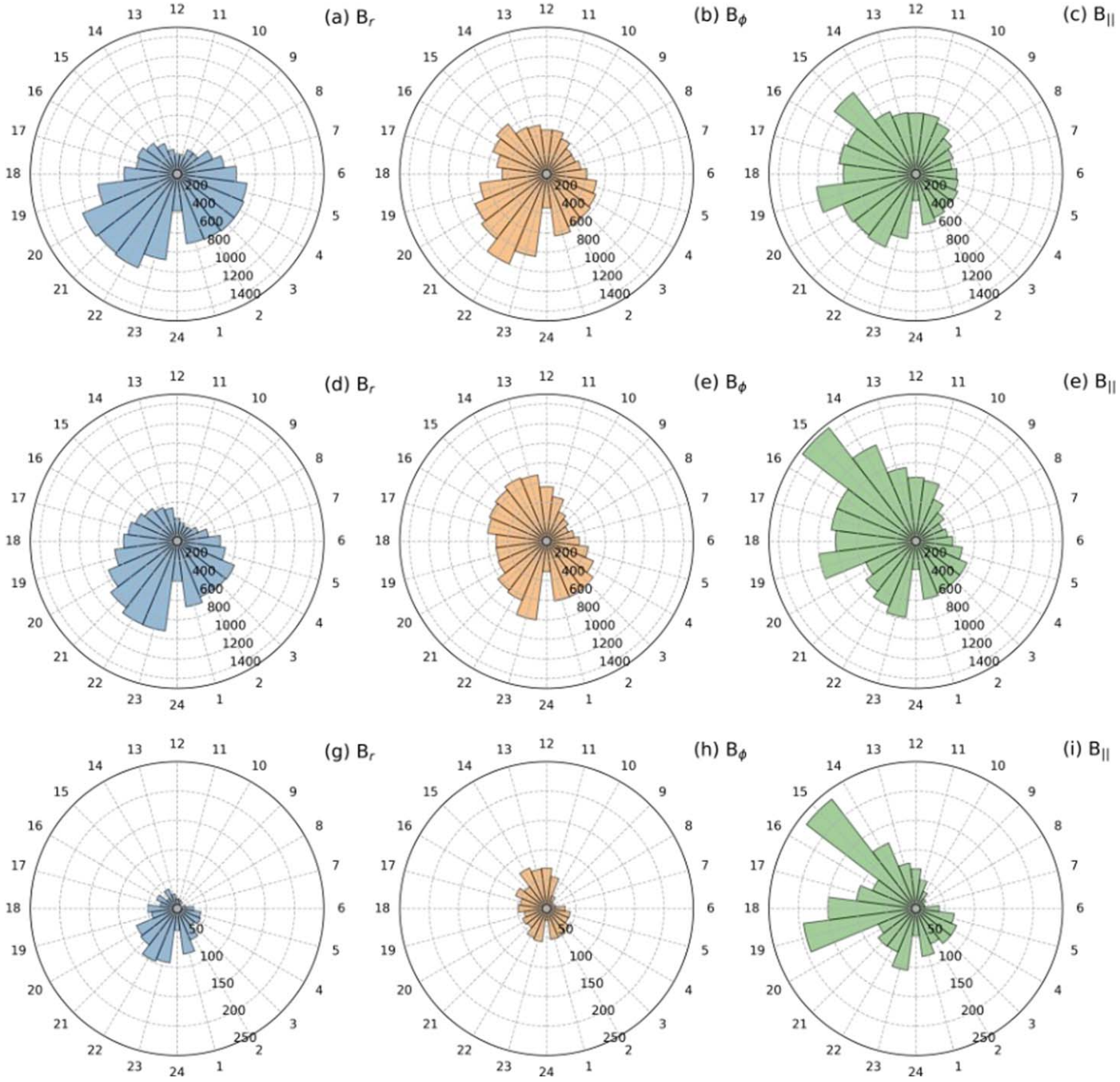

Figure 6. Occurrence rates for different by solar wind speeds: (a)–(c) for high speed $V_{sw} \geqslant 500$ km s^{-1}, (d)–(f) for moderate speed 500 km s^{-1} $> V_{sw} >$ 350 km s^{-1}, and (g)–(i) for low speed $\leqslant 350$ km s^{-1}.

0° and 180°, with most events roughly evenly distributed between about 40° and 140°.

5. Discussion

In this study, we introduced the CLEAN algorithm to the detection of ULF waves in Earth's magnetosphere. The method allows for identification of multiple individual peaks within the same PSD and produces real amplitudes instead of model fits. As shown in Figure 1, the method literally cleans the PSD by iteratively removing each peak in power after the spectral information is registered. The choice of the spectral width to remove is somewhat arbitrary, but it should be chosen to be wide enough to remove shoulder effects, while being careful not to remove nearby peaks. Of course, a secondary peak could be on the shoulder of the primary peak being analyzed. However, in that case it is unlikely that any methodology could clearly distinguish the two peaks' entire spectral information.

We cannot rule out some double counting of wave events due to the 30 minute overlap in the FFT sliding window but this should not change the relative statistics of the occurrence and amplitudes across MLT. Furthermore, having no overlap would introduce unwanted spectral artifacts, and employing an overlap is ubiquitous in spectral analysis. Since the CLEAN method identifies multiple peaks within the same FFT, it is inevitable that some harmonic peaks detected will be due to

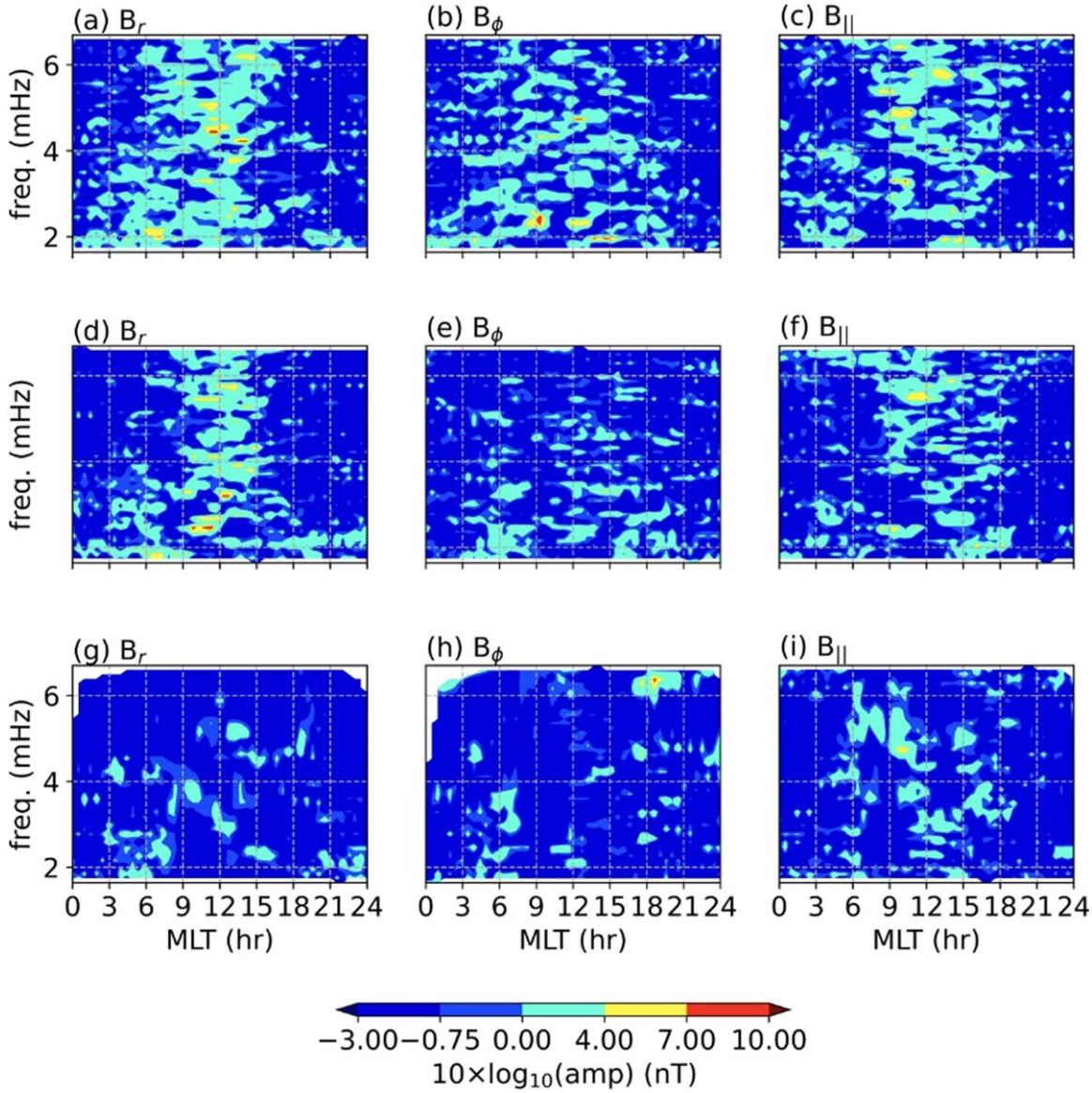

Figure 7. Amplitudes for different solar wind speeds: (a)–(c) for high speed $V_{sw} \geqslant 500$ km s^{-1}, (d)–(f) for moderate speed 500 km s$^{-1} > V_{sw} > 350$ km s^{-1}, and (g)–(i) for low speed $\leqslant 350$ km s^{-1}.

aliasing and Gibbs phenomena. Even with the Hanning window applied, we cannot completely avoid the problem without severely deforming the spectral signal. In fact, we found that if the Hanning window was removed, the number of events detected by the CLEAN method increased by threefold, and analysis of those additional events concluded that they were most likely artificial.

The results of the CLEAN method analysis are consistent with some previous Pc5 ULF wave statistical studies. For example, our results show that the 18–23 MLT quadrant has the highest overall occurrence of narrowband Pc5 waves, in agreement with Murphy et al. (2020b), who used 4 yr of GOES observations. Studies show (Mende et al. 2003; Frey et al. 2004; Gérard et al. 2004) that substorm onset tends to brighten initially in the pre-midnight sector, near 23 MLT, but onsets can occur between 20 and 02 MLT. Substorms tend to be accompanied by broadband signatures, although peaks at specific frequencies can still occur.

The Pc5 narrowband ULF wave amplitudes are predominantly restricted to the dayside in Earth's magnetosphere. This is not unexpected, because on the nightside, the field line footprints in the ionosphere are loose due to there being less ionospheric conductivity, and therefore narrowband pulsations such as field line resonances are not as common on the nightside. The nightside is mainly composed of broadband irregular pulsations, which often have low amplitudes except during short-duration bursts associated with substorms and bursty bulk flows.

Murphy et al. did not observe the increase in $B_{||}$ wave events at 15 and 19 MLT. We have no explanation for this observation. It is unlikely to be related to data issues, because the occurrence values at these two MLTs increased/decreased under different solar wind conditions just like the occurrences at other MLTs. If these spikes were due to artificial signals, then we would expect the values to be independent of solar wind conditions, unless the cause of the data issues was somehow related to space weather induced contamination.

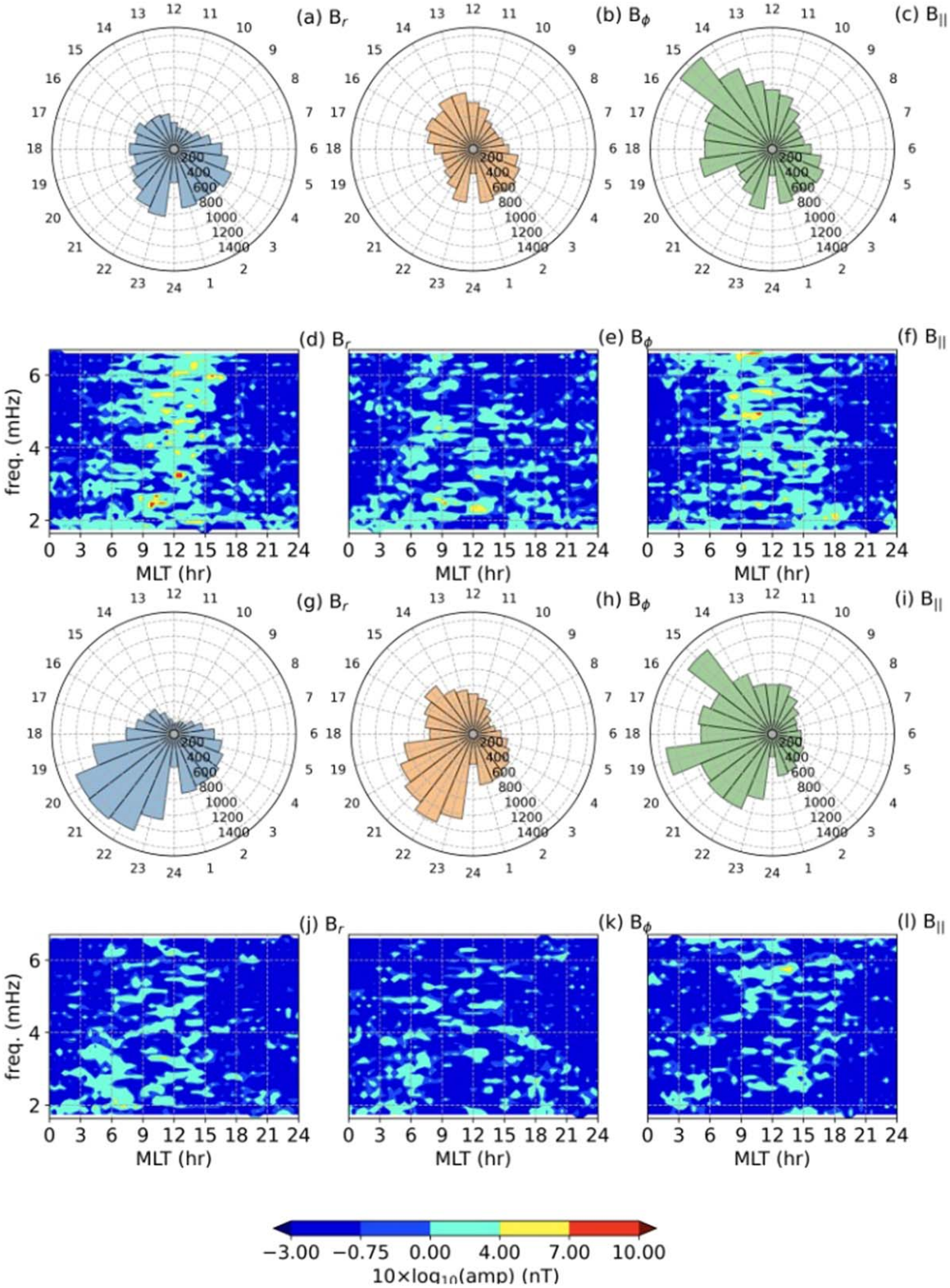

Figure 8. Occurrence rates for different solar wind densities: (a)–(f) for high densities $\geqslant 7/\mathrm{cm}^{-3}$ and (g)–(l) for lower densities $<7/\mathrm{cm}^{-3}$.

The minimal occurrence for B_r at around 09–12 MLT (see Figure 3(a)) is in contrast to the location of peak amplitudes, which occurs in the 09–15 MLT sector during more active solar wind conditions. Murphy et al. (2020b) also observed a decrease in the number of narrowband events at 10–12 MLT in the poloidal mode, but it was not the minimal local time. Differences between our results and those of Murphy et al. might be due to our study using a much larger data set, spanning decades, compared to Murphy et al. using 4 yr of data. These pronounced amplitudes around local noon during enhanced solar cycles, solar wind speeds, and densities align with the mechanism of solar wind pressure variations driving

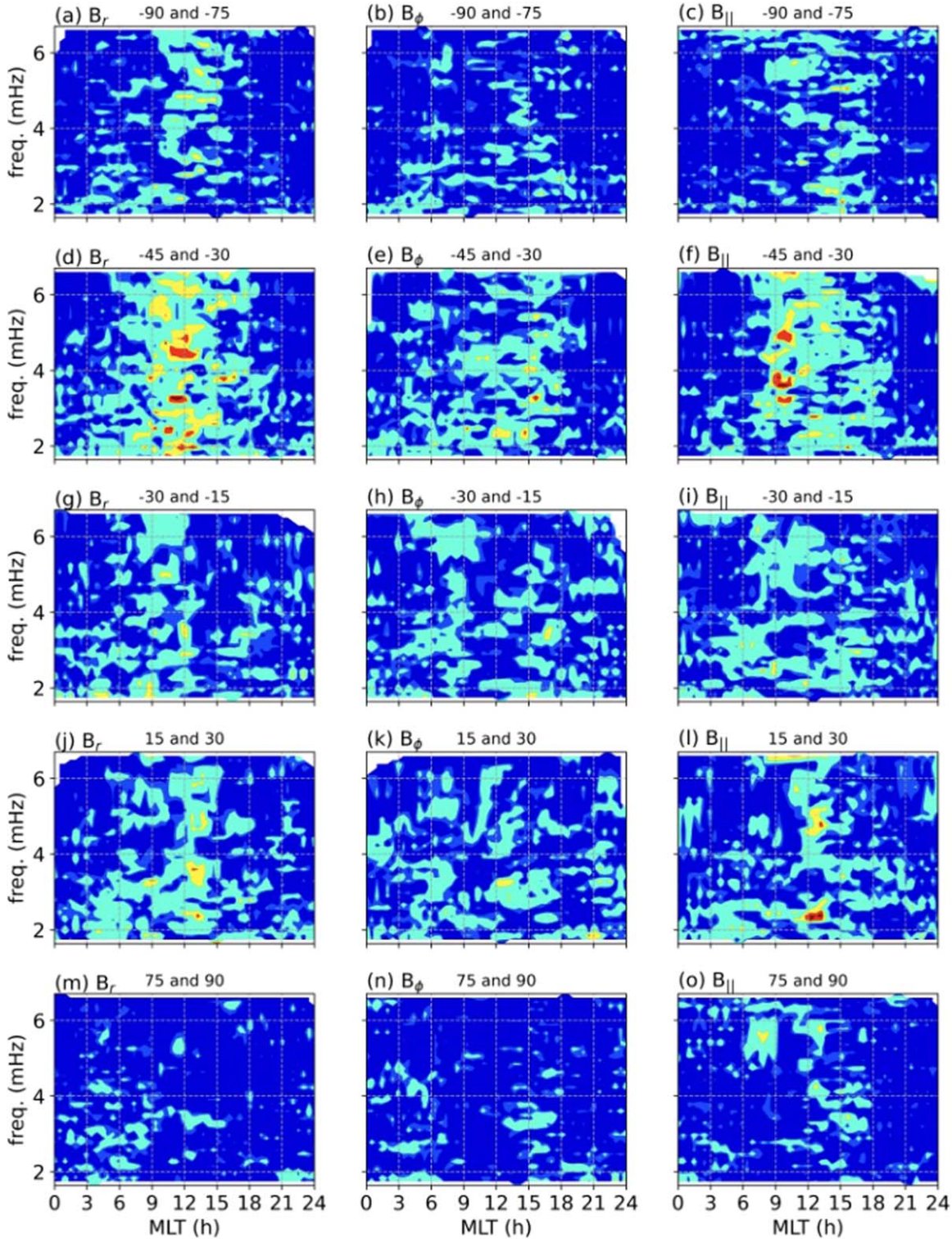

Figure 9. Pc5 wave amplitudes for different IMF 15° clock angles.

radial perturbations in Earth's magnetosphere (e.g., Takahashi & Ukhorskiy 2007). The $B_{||}$ component, in particular during SC-23 (see Figure 4), also saw pronounced amplitudes in the 09–15 MLT sector, in particular at higher frequencies. This may indicate that a significant contribution to $B_{||}$ comes from harmonic poloidal mode oscillations.

Murphy et al. found no clear evidence for an enhancement in narrowband Pc5 waves both on the dawn and dusk flanks, as expected for ULF waves externally driven by the Kelvin–Helmholtz instability (KHI; Wright & Mann 2006). This is generally true for the results in this study. However, we did find some evidence of preferences for amplitudes outside the local 06–12 MLT region at low frequencies for B_ϕ and B_{ll} (see Figures 3(e), 3(f), 5(k), and 5(l)). In Figure 5, this preference was observed during the weaker solar cycle. This effect was also observed for 75°–90° clock angles. At the

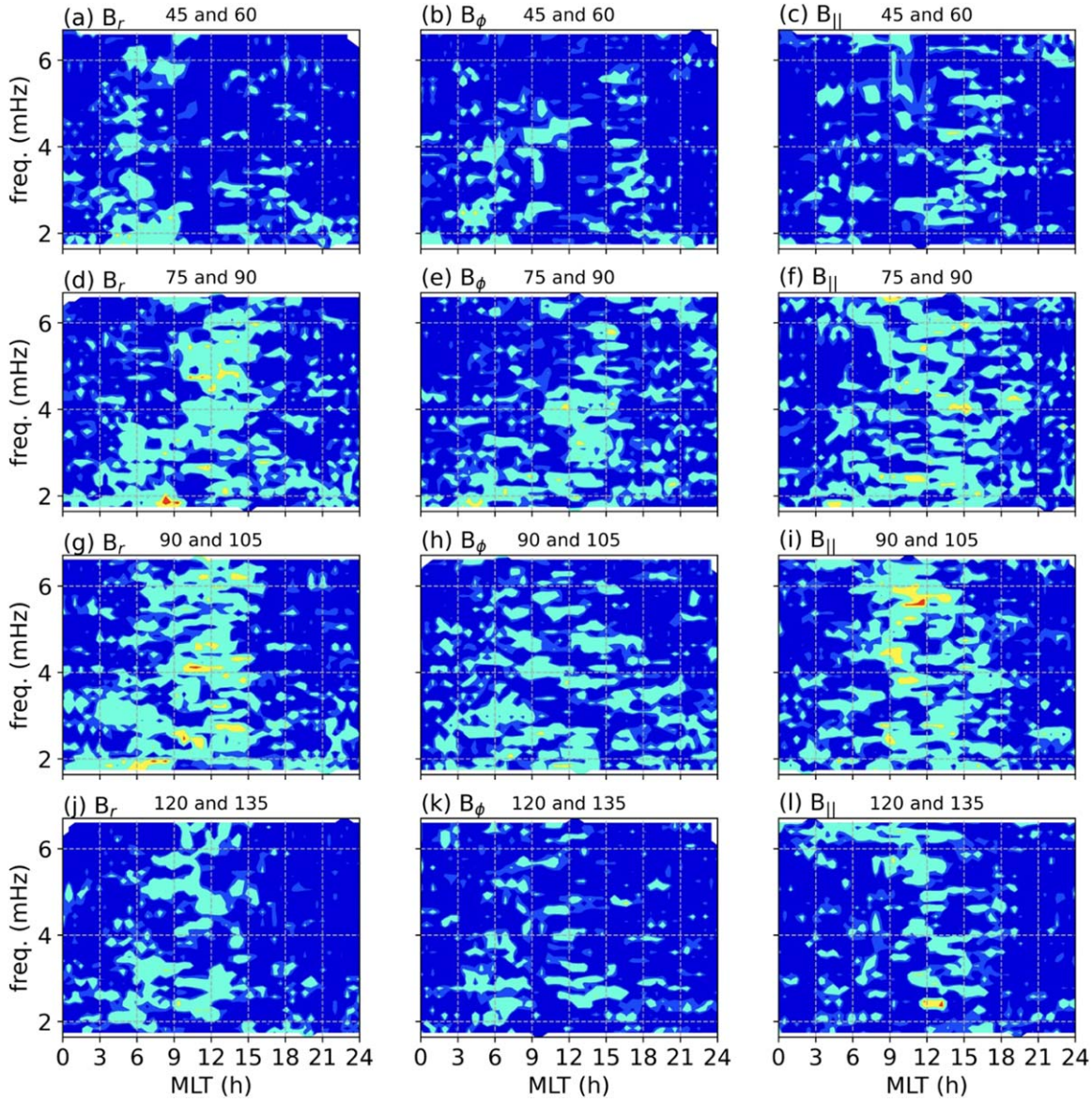

Figure 10. Pc5 wave amplitudes for different IMF 15° cone angles.

lowest frequencies, the B_r shows a tendency toward less power in the 09–18 MLT sector, with this effect again being more obvious during weak solar wind conditions.

Mathie & Mann (2000) found that morning-sector wave events occurring during high speed solar wind ($V_{sw} \sim 500\,km\,s^{-1}$) were likely driven by magnetopause flow instabilities such as KHI, while for lower solar wind speeds, ULF pulsations were likely related to impulsive solar wind events. However, in terms of amplitudes, we find that high-speed solar wind maximizes amplitudes close to local noon. We suggest that the lack of clear preference at the dawn and dusk flanks during more active periods is probably due to the dominance of radial variations near local noon caused by increased buffering by the solar wind on the magnetosphere. These larger-amplitude B_r can then couple to B_ϕ, filling in the azimuthal amplitude near local noon, while at the same time, stronger poloidal oscillations results in increased $B_{||}$ amplitudes also near local noon.

The fact that ULF amplitudes peak during negative IMF clock angle is not surprising, since an important factor in the geoeffectiveness of the solar wind is the southward component of the IMF. The IMF clock angle is usually connected to the rate of dayside reconnection and controls the magnetic field convection in the magnetosphere (Sonnerup 1974; Kan & Lee 1979). The "Russell–McPherron" (R–M) effect (Russell & McPherron 1973), where the difference between the GSM and GSE frames results in an in-ecliptic ± IMF by GSE component giving rise to a ± IMF B_z, leads to seasonal biases in the clock angle distribution and is most prominent around the equinoxes, with a maximum difference between Z_{GSM} and Z_{GSE} of ±34°.5 (Lockwood et al. 2016). This is consistent with the −45° to −30° clock angles where the total Pc5 wave amplitudes were generally observed to be highest.

We also looked at occurrence of the Pc5 waves with clock and cone angle (results not shown). Enhanced occurrence of Pc5 events with cone angle is spread over a wide angle range (40° to 140°), while for the clock angle, the occurrence peak/trough is more localized near ±90°. These results reflect how often certain clock and cone angles occur over a solar cycle (Fadiyah & Herdiwijaya 2022). However, Hartinger et al. (2013) found that cone angle is not the best indicator of Pc5

wave activity. The results presented here also suggest that IMF clock angle is a better indicator of Pc5 wave activity. We expect on average for the solar wind Parker spiral at Earth to make a 45° angle with the Sun–Earth line and lie roughly in the ecliptic plane, which translates to a 45° cone angle and 0° clock angle (in our definition), before the R–M effect is considered.

Finally, we studied the Pc5 occurrence and amplitudes as a function of day of the year (results not shown). Both the parallel and azimuthal components showed a clear maximum occurrence near the September equinox, and a smaller peak during March equinox. The occurrence rate of the radial Pc5 magnetic field component with day of year was more normally distributed with maximum around midyear or close to solace, although it did show elevated occurrences around the equinoxes. The Pc5 amplitude distributions show less clear association with the equinoxes, although the amplitudes of all three components were observed to increase during the equinoxes. In fact, all three components showed maximum wave amplitude closer to solace.

ULF wave–particle interactions resulting in particle radial diffusion is thought to play an important role in the dynamics of relativistic electrons in the radiation belts. The diffusion mechanism has been described as drift-resonant interaction where waves with frequencies comparable to the electron Earth orbit drift frequencies (or harmonics) can resonate with the electrons, causing the electrons to diffuse in the radial direction, which results in electron energy change due to conservation of the third adiabatic invariant (e.g., Faelthammar 1968; Schulz & Lanzerotti 1974; Elkington et al. 2003; Fei et al. 2006). The diffusion equation can be simplified into two terms (Fei et al. 2006), one representing diffusion due to the magnetic field, D_{LL}^{B}, and the other diffusion due to the electric field, D_{LL}^{E}. The magnetic field used in the calculation of D_{LL}^{B} is the compressional or parallel $B_{||}$ magnetic field component.

All else being kept constant, the wave frequency defines the minimum resonant energy of electrons for the drift-resonant mechanism, while the diffusion rate is proportional to the wave power. The results presented in this study of the distribution of Pc5 $B_{||}$ component amplitudes in frequency and MLT provides data to help constrain this drift-resonant interaction. We can calculate the energies for relativistic electrons to drift-resonate with ULF waves using the analytical relation from Ozeke & Mann (2008). Assuming a Pc5 wave frequency of 6.5 mHz, azimuthal wavenumbers of $m = 1$–3 and a 90° pitch angle, the resonant energies with relativistic electrons would range from 3.2 to 10.4 MeV at $L = 6.6$. However, as shown in Figure 4(f), the larger amplitudes are mainly restricted to higher $B_{||}$ wave frequencies and at the dayside close to local noon. In the case of outward radial diffusion of electrons, the ultrarelativistic electrons would diffuse and be lost to the dayside magnetopause faster at local noon than lower-energy electrons, due to the larger amplitudes at higher frequencies. However, when averaged across all local times and solar wind conditions (results not shown) amplitudes generally decrease with increasing frequency.

The Pc5 $B_{||}$ amplitudes being restricted during more active solar wind periods to 03–18 MLT indicates that radial diffusion of relativistic electrons is asymmetric as the electrons drift around Earth. The diffusion rate is maximum on the dayside, then decreases and minimizes through most of the local night time sector. Radiation belt models should account for this uneven diffusion with local time. In particular, the average amount of diffusion during one electron drift orbit will be lower than the values estimated by assuming that the ULF amplitude was evenly distributed across all MLTs. However, this may be somewhat offset by the fact that $B_{||}$ occurrence maximizes in the 18–23 MLT region. A more complete picture of radial diffusion would be to define higher rates of diffusion across the 03–18 MLT sector and lower rates but, on average, more frequent wave–particle interactions through the 18–03 MLT sector.

The fundamental poloidal and toroidal Pc5 ULF wave modes have a node at the magnetic dipole equator (Hughes 1994). GOES magnetometer data used in this study were mostly taken at the operational GOES-West and GOES-East locations, which corresponds to a geomagnetic dipole latitude of about 4° and 9°, respectively. Sarris et al. (2022) found that magnetic ULF wave power in the radial and azimuthal components increases away from the magnetic equator. Although observations of fundamental ULF modes are possible at the operational orbit of GOES, the measured fundamental mode amplitudes are unlikely to be the peak amplitude of the wave. This should be taken into consideration when studying wave–particle interactions in the radiation belt using GOES magnetometer data. However, solar wind–magnetospheric interactions can cause the minimal magnetic field strength (local magnetic equator) to offset or extend away from the dipole equator (Shabansky 1971), while magnetometers never observe completely pure modes in the magnetosphere.

Previous Pc5 ULF waves studies, mostly through ground observations, have observed preferred or "magic" frequencies (e.g., Rostoker & Samson 1972; Samson et al. 1991, 1992; Walker et al. 1992; Ziesolleck & McDiarmid 1994; Villante et al. 2001). In terms of in situ studies, Viall et al. (2009) used 10 yr of GOES magnetometer data and found that certain frequencies occurred more often than others. Magic frequency events are ascribed to magnetospheric cavity or waveguide modes. However, all our amplitude spectra show artificial horizontal streak-like patterns (e.g., see Figures 3(d), (e), and (f)) created by the discrete nature of the FFT, where spectral values are separated by the frequency resolution, which in our case is 0.28 mHz. This appearance remains despite the application of nearest-neighbor smoothing to the spectra. Although we observe some evidence in the peak amplitudes of preferred frequencies, such as in Figures 9(d) and (f), further discussion on this topic is beyond the scope of the current study.

6. Conclusions

The CLEAN algorithm was successfully applied to the detection of narrowband ULF waves in Earth's magnetosphere. Using GOES magnetometer data spanning over 30 yr, close to 30,000 events were found in each magnetic field component. The large database of events includes wave spectral properties and event date/time, which can be utilized for the study of Pc5 ULF wave characteristics and generation mechanisms and to study Pc5 ULF wave–particle interactions in the radiation belts. With some exceptions, results were generally in agreement with previous studies.

Acknowledgments

P.T.M.L. and F.I. are supported by the NOAA cooperative agreements NA17OAR4320101 and NA22OAR4320151. The

views, opinions, and findings contained in this report are those of the authors and should not be construed as an official National Oceanic and Atmospheric Administration, National Aeronautics and Space Administration, or other U.S. Government position, policy, or decision.

References

Anderson, B. J., Engebretson, M. J., Rounds, S. P., Zanetti, L. J., & Potemra, T. A. 1990, JGRA, 95, 10495
Cao, M., McPherron, R. L., & Russell, C. T. 1994, JGRA, 99, 8731
Cornwell, T. J. 2009, A&A, 500, 65
Elkington, S. R., Hudson, M. K., & Chan, A. A. 2003, JGRA, 108, 1116
Fadiyah, A., & Herdiwijaya, D. 2022, JPhCS, 2243, 012011
Faelthammar, C. G. 1968, in Proceedings of the NATO Advanced Study Institute, Earth's Particles and Fields, ed. B. McCormac (New York: Reinhold Book Corporation), 157
Fei, Y., Chan, A. A., Elkington, S. R., & Wiltberger, M. J. 2006, JGRA, 111, A12209
Frey, H. U., Mende, S. B., Angelopoulos, V., & Donovan, E. F. 2004, JGRA, 109, A10304
Gérard, J.-C., Hubert, B., Grard, A., Meurant, M., & Mende, S. B. 2004, JGRA, 109, A03208
Hartinger, M. D., Turner, D. L., Plaschke, F., Angelopoulos, V., & Singer, H. 2013, JGRA, 118, 299
Högbom, J. A. 1974, A&AS, 15, 417
Hudson, M. K., Denton, R. E., Lessard, M. R., Miftakhova, E. G., & Anderson, R. R. 2004, AnGeo, 22, 289
Hughes, W. J. 1994, in Magnetospheric ULF Waves: A Tutorial with a Historical Perspective, ed. M. J. Engebreston, K. Takahashi, & M. Scholer (Washington, D. C.: American Geophysical Union)
Inceoglu, F., & Loto'aniu, P. T. M. 2021, SpWea, 19, e2021SW002892
Inglis, A. R., Ireland, J., Dennis, B. R., Hayes, L., & Gallagher, P. 2016, ApJ, 833, 284
Inglis, A. R., Ireland, J., & Dominique, M. 2015, ApJ, 798, 108
Jacobs, J. A., Kato, Y., Matsushita, S., & Troitskaya, V. A. 1964, JGR, 69, 180
Kan, J. R., & Lee, L. C. 1979, GeoRL, 6, 577
Kokubun, S. 1985, JGG, 37, 759
Lessard, M. R., Hudson, M. K., & Lühr, H. 1999, JGRA, 104, 4523
Liu, W., Sarris, T. E., Li, X., et al. 2009, JGRA, 114, A12206
Lockwood, M., Owens, M. J., Barnard, L. A., et al. 2016, SpWea, 14, 406
Loto'aniu, T. M., Califf, S., Redmon, R. J., & Singer, H. J. 2019a, in The GOES-R Series, ed. S. J. Goodman et al. (Amsterdam: Elsevier), 251
Loto'aniu, T. M., Redmon, R. J., Califf, S., et al. 2019b, SSRv, 215, 32
Mathie, R. A., & Mann, I. R. 2000, JGRA, 105, 10713
Mende, S. B., Frey, H. U., Morsony, B. J., & Immel, T. J. 2003, JGRA, 108, 1339
Menk, F. W. 2011, in The Dynamic Magnetosphere, ed. W. Liu & M. Fujimoto (Dordrecht: Springer), 223
Murphy, K. R., Inglis, A. R., Sibeck, D. G., Watt, C. E. J., & Rae, I. J. 2020a, JGRA, 125, e27887
Murphy, K. R., Inglis, A. R., Sibeck, D. G., Watt, C. E. J., & Rae, I. J. 2020b, JGRA, 125, e2020JA027887
Ozeke, L. G., & Mann, I. R. 2008, JGRA, 113, A02201
Roberts, L. G., Lehar, I. R., & Dreher, J. W. 1987, AJ, 93, 968
Rostoker, G., & Samson, J. C. 1972, JGR, 77, 6249
Russell, C. T., & McPherron, R. L. 1973, JGR, 78, 92
Samson, J., Greenwald, R., Ruohoniemi, J., Hughes, T., & Wallis, D. 1991, CaJPh, 69, 929
Samson, J. C., Harrold, B. G., Ruohoniemi, J. M., Greenwald, R. A., & Walker, A. D. M. 1992, GeoRL, 19, 441
Sarris, T. E., Li, X., Zhao, H., et al. 2022, JGRA, 127, e2022JA030469
Schulz, M., & Lanzerotti, L. J. 1974, Particle Diffusion in the Radiation Belts (Berlin: Springer)
Shabansky, V. P. 1971, SSRv, 12, 299
Singer, H. J., Matheson, L., Grubb, R., Newman, A., & Bouwer, S. D. 1996, Proc. SPIE, 2812, 299
Sonnerup, B. U. Ö 1974, JGR, 79, 1546
Takahashi, K., & Ukhorskiy, A. Y. 2007, JGRA, 112, A11205
Viall, N. M., Kepko, L., & Spence, H. E. 2009, JGRA, 114, A01201
Villante, U., Francia, P., & Lepidi, S. 2001, AnGeo, 19, 321
Walker, A. D. M., Ruohoniemi, J. M., Baker, K. B., Greenwald, R. A., & Samson, J. 1992, JGR, 97, 12187
Wang, G. Q., Zhang, T. L., & Ge, Y. S. 2015, JGRA, 120, 9281
Wright, A. N., & Mann, I. R. 2006, in Magnetospheric ULF Waves: Synthesis and New Directions, ed. K. Takahashi (Washington, D. C.: American Geophysical Union), 51
Zhu, X., & Kivelson, M. G. 1991, JGRA, 96, 19451
Ziesolleck, C. W. S., & McDiarmid, D. R. 1994, JGR, 99, 5817